International Journal of Power Electronics and Drive System (IJPEDS)
Vol. 17, No. 1, March 2026, pp. 155~167
ISSN: 2088-8694, DOI: 10.11591/ijpeds.v17.i1.pp155-167

Implementation of finite control set-predictive torque control based on the dSpace DS1104 controller

Rozana Alik[1], Nik Rumzi Nik Idris[1], Norjulia Mohamad Nordin[1], Tole Sutikno[2,3]
[1]Faculty of Electrical Engineering, Universiti Teknologi Malaysia, Johor, Malaysia
[2]Department of Electrical Engineering, Faculty of Industrial Technology, Universitas Ahmad Dahlan, Yogyakarta, Indonesia
[3]Embedded System and Power Electronics Research Group, Yogyakarta, Indonesia

Article Info

Article history:

Received Mar 5, 2024
Revised Jan 3, 2026
Accepted Feb 11, 2026

Keywords:

dSpace DS1104 controller
Flux ripple
Induction motor drives
Predictive torque control
Torque ripple

ABSTRACT

Finite control set-predictive torque control (FCS-PTC) has emerged as a popular control method for induction motors (IMs) over the past decade. This paper provides a detailed hardware implementation of FCS-PTC with a constant weighting factor (WF) on 186 W of IM. The FCS-PTC is implemented using the DS1104 controller board programmed using C code. A comprehensive analysis of flux, torque, and the total harmonic distortion (THD) of the stator current is conducted and presented to establish a relationship between the WF and drive performance. The experimental results indicate that a higher WF results in improved performance in flux and THD current, but a poorer torque response. Conversely, a lower WF improves torque performance but sacrifices the flux and THD current. The analysis outcome will hopefully provide some guidelines for developing the WF selection techniques.

Corresponding Author:

Rozana Alik
Faculty of Electrical Engineering, Universiti Teknologi Malaysia
81310 Skudai, Johor, Malaysia
Email: rozana.a@fke.utm.my

1. INTRODUCTION

Over the past few decades, three-phase induction motors (IMs) have found widespread application across various industrial sectors. The reason is mainly due to its durability, low maintenance needs, cost-effectiveness, and the ability to operate at higher speeds. However, achieving effective control of IMs is challenging due to the complexity of their dynamic models, and therefore, remains one of the hot research topics in motor drives. This topic has even attracted much attention from researchers due to the growing utilization of renewable energy and electric vehicles. Furthermore, advancements in microprocessors have provided researchers with an opportunity to develop more powerful control strategies.

Two main control strategies, namely field-oriented control (FOC) and direct torque control (DTC), are extensively employed in high-performance IM drive applications [1]. FOC utilizes a linear control strategy, which involves the utilization of a linear controller to generate a reference voltage, which is then implemented using a pulse width modulator (PWM) [2]. There are several types of FOC for IM drives, determined by the specific field to which the rotating frame is oriented. The most widely adopted type is the rotor flux FOC. In rotor flux FOC, the rotating frame aligns with the rotor flux, which rotates at synchronous speed. Within this frame, the stator current vector is decomposed into its flux and torque components, which are orthogonal and, therefore, are magnetically decoupled. An inner-current control loop with PWM is required to implement this control strategy. This current control needs to be implemented precisely to ensure optimal torque and flux control performance.

In contrast, DTC utilizes a pre-determined switching table and two hysteresis controllers to identify the optimal voltage vector (VV) selection for the IM [3]. Compared to the FOC, DTC has a simpler structure and does not require a modulator. DTC also offers simpler implementation and better resilience to parameter variations. However, its performance is highly influenced by the characteristics of the hysteresis controllers, which can cause high torque ripple and variable switching frequency [4]. Modified DTC methods [5]–[7] strive to address these limitations and, to a certain extent, have mitigated these issues. However, this improvement comes at the cost of a more intricate control structure and implementation.

Recently, the application of model predictive control (MPC) to the IM drives has gained a lot of attention among researchers [8], [9]. For power electronics converters with fixed switching states, a variation of the MPC known as finite control set-predictive torque control (FCS-PTC) technique, simplifies implementation and reduces execution time [10]. The optimization stage of FCS-PTC involves selecting a VV that minimizes a cost function. The two main variables that define the cost function of the FCS-PTC are the torque and flux. Since torque and flux are fundamentally different, employing a weighting factor (WF) to assign different priorities to these control variables is common. Thus, WF's selection affects the dynamic characteristics of the control variables and, hence, the drive performance. Therefore, this paper seeks to clarify the impact of WF selection on the control performance of the drive. The analysis is simplified through its implementation using a dSPACE controller board – details on the implementation using C codes are discussed and presented in this paper.

2. MODELLING A THREE-PHASE INDUCTION MOTOR

A more compact and convenient way of modelling a symmetrical three-phase system is to use space vector (also known as space phasor) equations. By expressing the three-phase IM using space vector equations as in (1) to (5), the analysis of a symmetrical three-phase IM becomes more straightforward [11], [12].

$$v_s = i_s R_s + d\psi_s/dt \tag{1}$$

$$0 = i_r R_r + d\psi_r/dt - j\omega_r \psi_r \tag{2}$$

$$\psi_s = L_s i_s + L_m i_r \tag{3}$$

$$\psi_r = L_r i_r + L_m i_s \tag{4}$$

$$T_e = (3p/2)\Im\mathfrak{m}(i_s \psi_s^*) \tag{5}$$

Where v_s, ψ_s, ψ_r are the stator voltage, stator flux, and rotor flux space vectors, respectively. Also T_e is the electromagnetic torque (expressed in terms of stator current and stator flux space vectors) and, R_s and R_r are the stator and rotor resistances, respectively. Meanwhile, the stator and rotor current space vectors are represented as i_s and i_r. Next, L_s, L_r and L_m indicated the stator self-inductance, rotor self-inductance, and mutual inductance, respectively. Lastly, the ω_r is the electrical rotor speed, and the pair of poles is labelled as p.

The stator and rotor currents, as in (6) and (7) can be obtained by manipulating (3) and (4). Meanwhile, (5) can be expressed in terms of the d-q quantities (scalar) as in (8) for the torque. All of these equations are used for the estimation and predictions of control parameters in FCS-PTC.

$$i_s = [1/(L_s L_r - L_m^2)]\,(L_r \psi_s - L_m \psi_r) \tag{6}$$

$$i_r = [1/(L_s L_r - L_m^2)]\,(L_s \psi_r - L_m \psi_s) \tag{7}$$

$$T_e = (3p/2)\,[(\psi_{sd} i_{sq}) - (\psi_{sq} i_{sd})] \tag{8}$$

3. MODELLING A THREE-PHASE VOLTAGE SOURCE INVERTER

Figure 1(a) depicts a two-level, three-phase voltage source inverter (VSI) utilizing six insulated-gate bipolar transistors (IGBTs) for power switches, with an input voltage V_{DC} and the output connected to a three-phase IM. Each IGBT, labelled Q_1 through Q_6, possesses an internal anti-parallel diode to offer a freewheeling path for the current when the IGBT is turned off.

The output voltage of the space vector that is applied to the IM is controlled by adjusting the switching states of the power switches. While modulators are commonly used, the output voltage of a VSI can also be controlled by directly controlling the switching states of the power switches without requiring a modulator. Likewise, PTC utilizes an optimization stage within the algorithm to determine the appropriate VVs, which is translated into switching states.

Figure 1(b) illustrates the VVs for a two-level three-phase VSI, which consists of six active VVs (v_1 - v_6) and two zero VVs (v_0 and v_7). These VVs can be resolved into their respective d and q components, as listed in Table 1. Using a 3–phase VSI, eight possible switching states (or VVs) can be implemented. The (9) describes the mathematical relationship between the output voltage (stator voltage) space vector and the switching states of the VSI. In this equation, V_{dc} represents the input DC link voltage to the VSI, while the switching states of each leg are represented by S_A, S_B, and S_C. The upper switch of a leg being ON corresponds to a switching state of 1, while the lower switch of a leg being ON corresponds to 0.

$$\mathrm{v_s} = 2/3\,\mathrm{V_{dc}}(\mathrm{S_A} + \alpha \mathrm{S_B} + \alpha^2 \mathrm{S_C}) \tag{9}$$

Where, $\alpha = e^{j\frac{2\pi}{3}}$ and $\alpha^2 = e^{j\frac{4\pi}{3}}$.

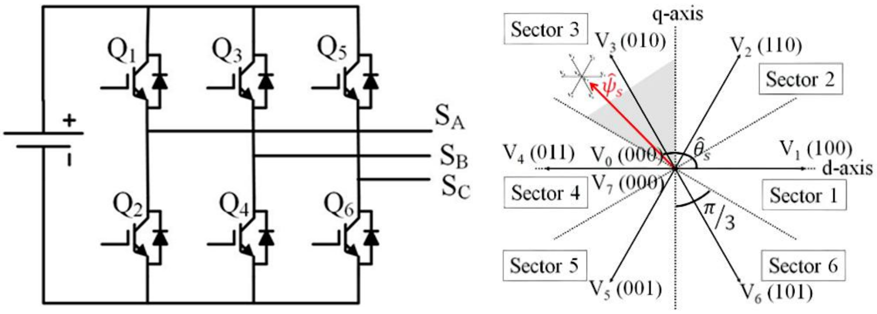

(a) (b)

Figure 1. VSI configuration

Table 1. Voltage vectors for each switching states of 2L VSI

v_n	$S = [S_A S_B S_C]$	$v_s = v_d + jv_q$
v_0	000	0
v_1	100	$(2/3)V_{dc}$
v_2	110	$\left(1/3 + j\sqrt{3}/3\right)V_{dc}$
v_3	010	$\left(-1/3 + j\sqrt{3}/3\right)V_{dc}$
v_4	011	$-(2/3)V_{dc}$
v_5	001	$\left(-1/3 - j\sqrt{3}/3\right)V_{dc}$
v_6	101	$\left(1/3 - j\sqrt{3}/3\right)V_{dc}$
v_7	111	0

4. FINITE CONTROL SET - PREDICTIVE TORQUE CONTROL

Figure depicts the block diagram of FCS-PTC. It comprises three significant stages [9], [10]: estimation, prediction and optimization.

4.1. Estimation

Estimating stator flux in IMs is crucial for any control strategies. Traditionally, voltage-based models were employed due to their simplicity [13], [14]. However, limitations like inverter nonlinearities and current measurement errors led to offset issues. Consequently, current-based models have gained favor [15]–[17]. To estimate the stator flux, the rotor flux equation in (2) is discretized using forward Euler's equation method, thus giving (10).

$$\hat{\psi}_r(k) = \hat{\psi}_r(k-1) + T_s\left[R_r L_r L_m i_s(k) - (1/(R_r L_r) - jp\omega(k))\hat{\psi}_r\,(k-1)\right] \tag{10}$$

Where, T_s is the sampling time. Finally, the stator flux, $\hat{\psi}_s$, is estimated using the flux linkage equations in (3) and (4), resulting in (11).

$$\hat{\psi}_s(k) = (L_m/L_r)\,\hat{\psi}_r(k) + i_s(k)\left(L_s - {L_m}^2/L_r L_s\right) \tag{11}$$

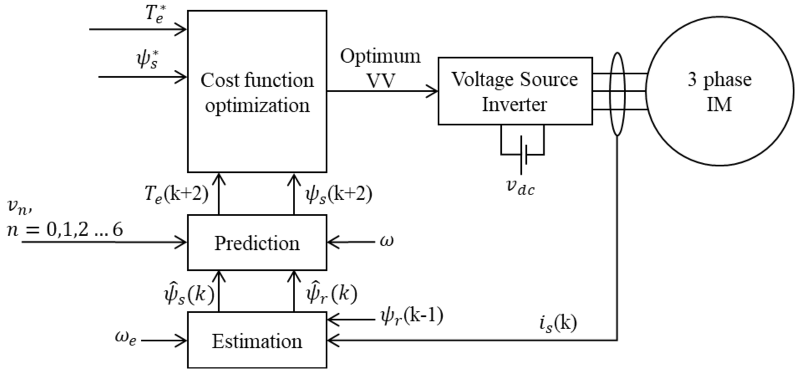

Figure 2. A detailed block diagram of FCS-PTC

4.2. Prediction

The prediction stage requires predicting two variables: stator flux and torque. By applying Euler discretization on (1), the stator flux can be predicted using (12).

$$\hat{\psi}_s^p(k+1) = \hat{\psi}_s(k) + T_s v_s - R_s i_s(k) \tag{12}$$

The (5) shows the direct relationship between torque prediction and stator flux and current. Therefore, the torque prediction is expressed using the predicted stator flux and current values as (13). To predict the torque, a prediction of the stator current $\hat{i}_s^p(k+1)$ is required (as seen in (13)). It can be shown that the stator current of IM can be expressed as (14) [18], [19].

$$T_e^p(k+1) = 3p/2\,\Im\mathfrak{m}\left[\hat{\psi}_s^p(k+1)\,\hat{i}_s^p(k+1)\right] \tag{13}$$

$$i_{\boldsymbol{s}}^{\boldsymbol{p}}(k+1) = (1 + T_s/\tau_\sigma)\boldsymbol{i_s}(k) + T_s/\tau_\sigma + T_s\left[1/R_\sigma\left[(k_r/\tau_r - k_r j\omega)\hat{\psi}_{\boldsymbol{r}}(k) + v_s(k)\right]\right] \tag{14}$$

In (14), τ_σ represents the transient time constant of the stator, k_r is the rotor coupling factor and τ_r is the rotor time constant.

Inevitably, the sampling process introduces a delay in hardware implementation [10], [20]. Therefore, the predicted torque and flux require a delay compensation which can be obtained by extending the predictions of torque and flux to the next sampling time (k + 2), using the (k + 1) values as the initial values. Finally, in (15)-(17) show the predicted torque and flux expressions.

$$\hat{\psi}_s^p(k+2) = \hat{\psi}_s(k+1) + T_s v_n - R_s i_s(k+1) \tag{15}$$

$$i_{\boldsymbol{s}}^{\boldsymbol{p}}(k+2) = (1 + T_s/\tau_\sigma)i_s(k+1) + T_s/(\tau_\sigma + T_s)\left[1/R_\sigma\left[(k_r/\tau_r - k_r j\omega)\hat{\psi}_{\boldsymbol{r}}(k+1) + v_s(k)\right]\right] \tag{16}$$

$$T_e^p(k+2) = 3p/2\ \Im\mathfrak{m}\left[\hat{\psi}_s^p(k+2)\,\hat{i}_s^p(k+2)\right] \tag{17}$$

In this work, only one of the two zero VVs is selected since this will simplify the implementation. As far as the torque and flux responses are concerned, both vectors (v_0 and v_7) will produce the same effect. Therefore, whenever zero VV is selected, v_0 will be used. Subsequently, only seven VV are used in the implementation, which are v_0, v_1, v_2, v_3, v_4, v_5, and v_6.

4.3. Optimization

The optimization stage is performed by minimizing the cost function. In (18) shows a typical cost function for FCS–PTC, which is used in this paper.

$$g = \left|T_e^* - T_e^p\ (k+2)\ \right| + \lambda_\psi\left|\ \psi_s^* - \psi_s^p(k+2)\right| \tag{18}$$

In this equation, T_e^* and ψ_s^* are the reference torque and reference stator flux and λ_ψ is the flux WF which determines the significant of stator flux error relative to the torque error. The cost function calculates the errors between the torque and flux references and their predicted values for every possible VV. The VV that gives the smallest value of the cost function is then selected and implemented using the VSI based on (9) and Table 1.

The WF plays a crucial role in the cost function in determining the relative importance of torque and flux control in PTC of IMs [21]. The control variables (i.e. flux and torque) in the cost function have different types in terms of units and magnitudes, so a WF is utilized to ensure fair optimization. However, selecting the WF value is not simple, even with the simple and intuitive idea of PTC and its capability to handle nonlinearity and constraints, especially when the control variables are of equal importance [17], [21]–[23]. For example, if λ_ψ is set to a relatively high value, then a higher priority will be given to the flux control instead of the torque control, and this, in turn, can cause higher torque ripple. If, on the other hand, λ_ψ is selected to be too low, then more priority will go to torque control, which can cause unnecessarily high flux ripple. Furthermore, the selection of WFs depends on the operating conditions [24]. This paper will highlight the significance of this inference by implementing the FCS-PTC with a very low λ_ψ of 5 and a relatively high λ_ψ of 30.

5. HARDWARE IMPLEMENTATION AND C PROGRAM DEVELOPMENT

Figure 3 displays the hardware setup in this paper. It comprises a DS1104 controller board from dSPACE, speed encoder, IM, gate drivers, 3 phase VSI, current sensors, and a DC power supply. The FCS-PTC control algorithm is implemented to a 186 W, 1425 rpm, three-phase squirrel cage IM as shown in Figure 3. An incremental speed encoder with 2048 pulses per revolution sampled at 0.001s is used to monitor and measure the motor speed. Detailed parameters for the IM can be found in Table 2. Figure 4 provides an overview of the interconnected components and their interactions within the hardware implementation.

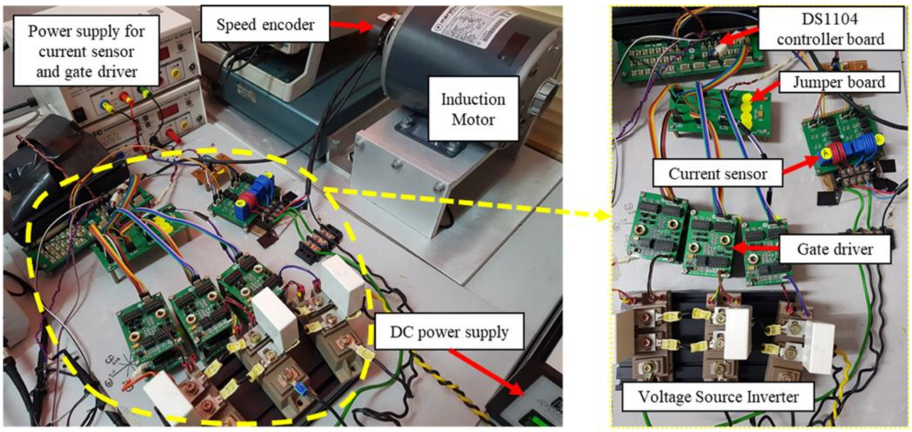

(a) (b)

Figure 3. Hardware setup for the drive system: (a) full view of the whole setup and (b) zoom view for interconnected components

Table 2. Specifications and parameters of the induction motor

Induction motor parameters		
Parameter	Symbol	Value
Rated power	P_{rated}	186 W
Rated speed	ω_{rated}	1425 RPM
Rated frequency	f	50 Hz
Rated line voltage	$V_{LL,\ rated}$	190 V
Rated current	I_{rated}	1.4 A
Pole pairs	p	2
Stator resistance	R_s	9.9 Ω
Rotor resistance	R_r	8.15 Ω
Stator inductance	L_s	278.6 mH
Rotor inductance	L_r	285.3 mH
Mutual inductance	L_m	265.1 mH
Moment of inertia	J	0.001118 kgm^2
Viscous friction	B	0.0006076 Nms
Sampling time	T_s	40 µs

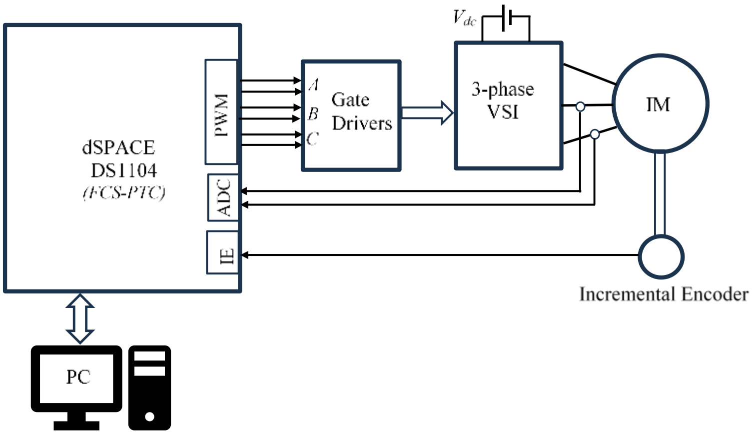

Figure 1. Functional block diagram of the hardware implementation

5.1. Current measurements

A pair of Hall-Effect current sensors as in Figure 3 are used to measure two of the stator currents of the IM. Based on (19) and (20), the Clarke transformation converts three-phase current measurements into two-phase currents in the dq-coordinate system. The 3 phase currents are then converted to 2 phase quantities (i_{sd} and i_{sq}):

$$i_{sd} = i_A \tag{19}$$

$$i_{sq} = (i_A + 2i_B)/\sqrt{3} \tag{20}$$

A ±12 V DC power supply powers the current sensor circuits. A current measurement of 50 A is required to give a full–scale deflection of 5 V at the output. Therefore, several turns of conductors are coiled at the core of each current sensor to improve measurement accuracy. Since DC offset in Hall sensor current measurement is inevitable, offsets are initially calculated before the interrupt service routine is started. This is performed by measuring the offsets for several thousand samples before the motor current starts to flow and then calculating the average value:

```
For i = 1 to n
{Measure the $i_{Ao}$ and $i_{Bo}$
$i_{AT} = i_{AT} + i_{Ao}$
$i_{BT} = i_{BT} + i_{Bo}$}
$offset_A = \frac{i_{AT}}{n}, offset_B = \frac{i_{BT}}{n}$
```

These offsets are then subtracted from the measured current when the motor currents are measured in the interrupt service routine:

```
Measure current $i_A$ and $i_B$
$i_A = i_A - offset_A$
$i_B = i_B - offset_B$
```

5.2. Gate drivers and blanking time

The gate driver board in Figure 3 increases the 5 V control signals from the DS1104 board to 15 V. It amplifies the low-power input from the controller to high-power output to provide enough voltage and current to turn on and turn off the IGBT modules. The upper and lower switching states of a leg for every phase are always complementary. In practice, there is a finite time for the IGBT to turn on (or turn off). Thus, to avoid short circuit in a leg of a phase, a blanking time of 3µs is inserted for each phase to ensure proper operation. The 3 phase PWM signals with blanking time can be generated using the PWM modulator that comes with the DSP subsystem (slave). However, in FCS–PTC, PWM modulator is not needed since the switching states, instead of duty cycles, are determined in the optimization stage. To make use of this feature, the duty cycles for the three phases PWM are changed to either 1 or 0 for every sampling time, depending on the selected voltage vector within each sampling time. For example, if the selected voltage vector is v_1 (i.e. 001) is selected, then the duty cycle of 0 for phase A, 0 for phase B and 1 for phase C are assigned. If VV_{min} is the selected voltage vector based on cost function minimization, then the following pseudo codes illustrates how the PWM modulator is used to produce the switching state for the VSI:

```
Initialize the slave DSP PWM communication:
Duty cycle for phase A = $duty_A$
Duty cycle for phase B = $duty_B$
Duty cycle for phase C = $duty_C$
blanking time is set to 3 µs
if($VV_{min}$ = $v_0$){
   $duty_A$ = 0; $duty_B$ = 0; $duty_C$ = 0;}
 else if($VV_{min}$ = $v_1$){
   $duty_A$ = 1; $duty_B$ = 0; $duty_C$ = 0;}
 else if($VV_{min}$ = $v_2$){
   $duty_A$ = 1; $duty_B$ = 1; $duty_C$ = 0;}
 else if($VV_{min}$ = $v_3$){
   $duty_A$ = 0; $duty_B$ = 1; $duty_C$ = 0;}
 else if($VV_{min}$ = $v_4$){
   $duty_A$ = 0; $duty_B$ = 1; $duty_C$ = 1;}
 else if($VV_{min}$ = $v_5$){
   $duty_A$ = 0; $duty_B$ = 0; $duty_C$ = 1;}
 else if($VV_{min}$ = $v_6$){
   $duty_A$ = 1; $duty_B$ = 0; $duty_C$ = 1;}
```

5.3. Three-phase VSI

The IGBT modules manufactured by Fuji Electric is utilized for the VSI in this paper, as shown in Figure 3. These modules have a rated voltage of 1200 V and a rated current of 100 A. Snubber circuits are incorporated across each IGBT module to protect the IGBT modules from voltage spikes and prevent damage due to rapid voltage rise. The snubber circuit provides an alternative path for the current when the IGBT switch is open. It effectively dampens the voltage transients and reduces stress on the IGBT module. These snubbers have a capacitance of 0.47 µF and a rated voltage of 1600 V.

5.4. Programming the DS1104 for FCS-PTC

The DS1104 is a controller board developed by dSPACE Inc. It comprises a master processor, the MPC8240 Power PC, and a slave-DSP subsystem that utilizes the TMS320F240 from Texas Instruments. Interfacing between the board and hardware is established through digital I/Os, as well as ADC and DAC channels provided on the board. In general, there are two methods available for programming the DS1104, which are described below:

i) By constructing the control algorithm using Simulink, which is then compiled and uploaded to the DS1104 for real–time execution. In this case, the interface between the board and the hardware is facilitated through the Simulink library provided by dSPACE. Consequently, there is no need for proficiency in a specific programming language to program the board. The C program is automatically generated from Simulink, compiled, and uploaded to the board, making it the simplest and quickest method for programming. However, it is important to note that the generated C program is not optimized, resulting in unnecessarily high sampling time and subsequently reducing the control bandwidth. For complex control algorithms, such as those encountered in FCS–PTC that contain multiple predictions and estimations, the sampling time can become unacceptably high.

ii) By manually writing C programs (hand coding) using C functions from the real-time library provided by dSPACE, the C codes are then compiled, linked, and uploaded to the DS1104. This method is undoubtedly more efficient than the previous one, as the C program is tailored to the specific needs. However, it comes with the drawback of being time-consuming and tedious.

When dealing with detailed control algorithms, such as FCS-PTC, the second method appeared to be the optimal choice. Employing the hand-coded C program enables achieving a remarkable sampling time of 40 µs something unattainable using Simulink. The interface between a user and the system is established via ControlDesk, a software provided by dSPACE. Within the ControlDesk environment, users can download applications to the DS1104, configure virtual instrumentation for monitoring purposes, and even perform real-time automation and controller fine-tuning.

In general, FCS-PTC consists of 3 stages: estimation, prediction and optimization – this has been discussed in the previous section. To implement the prediction and optimization stages, a loop structure is used.

As discussed earlier, to compensate for the delay due to the implementation, the prediction at the $(k+2)^{th}$ sample (instead of $(k+1)^{th}$) is used. The algorithm for the estimation, prediction and optimization stages is as follows:

```
Estimate the Torque and Stator Flux ($k^{th}$ sample) – equations (10) and (11)
Predict Torque and Stator Flux for $(k+1)^{th}$ sample – equations (12), (13) and (14)
For voltage vector = 0 to 6
Predict Torque and Stator Flux for $(k+2)^{th}$ sample, using $(k+1)^{th}$ values as the initial condition – equations (15), (16) and (17)
Calculate cost function based on equation (18)
Choose the voltage vector that gives minimum cost function, $VV_{min}$
Apply the $VV_{min}$ switching state to the VSI.
```

6. RESULTS AND DISCUSSION

This section will elaborate on the experimental results obtained for FCS-PTC using two different WF values. For clarity, the control drives are labelled as PTC5 and PTC30. PTC5 refers to FCS-PTC with a WF of 5, and PTC30 refers to FCS-PTC with a WF of 30.

6.1. Speed dynamic performance

The performance of PTC5 and PTC30 during acceleration (from a standstill) and speed reversal is analyzed to evaluate the speed dynamic characteristics. This is conducted by accelerating the motor from a standstill to its rated speed of 150 rad/s, followed by a speed reversal to 150 rad/s as shown in Figure 5. Both results demonstrate excellent dynamic performances for all methods. This observation suggests that the dynamic responses of the speed responses of all methods are comparable.

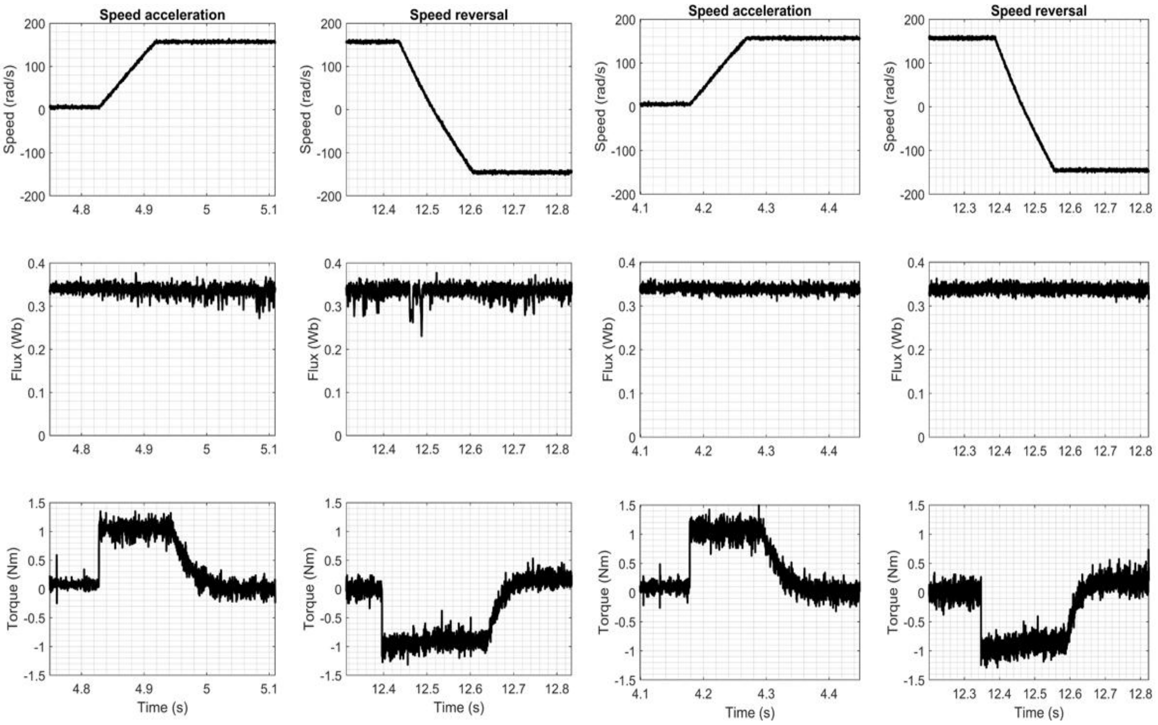

(a)

(b)

Figure 5. Speed acceleration and reversal performance: (a) PTC5 and (b) PTC30

6.2. Steady-state analysis

The steady-state performances of PTC5 and PTC30 are compared in terms of the flux and torque ripples and THD of the phase current (THD_I) at three different operating speeds of 30 rad/s, 80 rad/s, and 150 rad/s. Comparisons on flux and torque ripples are made based on the instantaneous waveforms of the flux and torque, and further analyzed using the flux and torque standard deviations as the performance index.

6.2.1. Flux response

The experimental results of the steady-state flux waveforms at these steady-state speeds are presented in Figure 6. It is observed that PTC5 has the poorest flux response. This occurred because of the relatively low flux control priority compared to the torque control. Specifically, the flux control is highly sensitive to the VV selection at low speeds. Consequently, the flux response is inferior to other methods, resulting in a distorted flux waveform. Nonetheless, as the speed increases, the flux response gets better.

For further analysis, each method calculates a standard deviation of the steady-state flux response, σ_ψ to analyze the ripples. Table 3 summarizes the experimental results at three steady-state speed settings of 30 rad/s, 80 rad/s, and 150 rad/s. The results indicate that at a speed of 30 rad/s, the PTC5 exhibits the highest σ_ψ, which is 0.0131. By implementing PTC30 with a high WF, which is 30 within the system, at least 35% reduction in σ_ψ is observed.

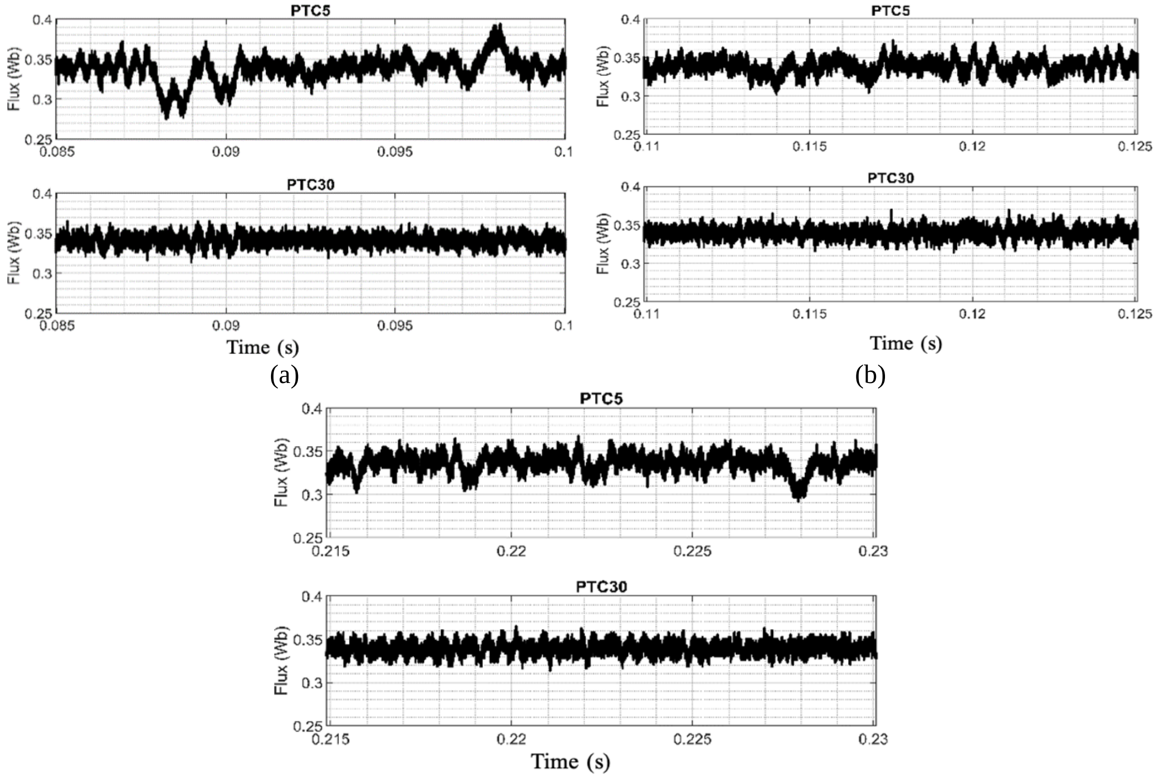

(a) (b)

(c)

Figure 6. Flux response for FCS-PTC with WF of 5 and 30 at different speeds:
(a) 30 rad/s, (b) 80 rad/s, and (c) 150 rad/s

6.2.2. Torque response

The experimental results of the torque waveforms at these steady-state speeds are presented in Figure 7. In order to further evaluate the steady state torque ripple, the standard deviation of the torque, σ_T for both schemes is evaluated and presented in Table 3, PTC5 produces the lowest σ_T at all speeds. However, PTC5 also, according to the previous discussion in section 6.1.1, PTC5 produces the highest flux ripple. Thus, a lower value of the WF can only fulfil the torque ripple requirement since more priority is given to the torque control than the flux control but, at the same time, sacrifices the flux control, thus resulting in a higher flux ripple. Nonetheless, PTC30 provides higher σ_T even though it has low flux ripple.

Table 3. Flux ripple, torque ripple, and current harmonic distortion for PTC5 and PTC30 under three different speeds

Speed (rad/s)	PTC5			PTC30		
	30	80	150	30	80	150
σ_ψ	0.0131	0.0115	0.0104	0.0065	0.0066	0.0067
σ_T	0.0101	0.0101	0.0998	0.1390	0.1410	0.1430
THD_I (%)	36.81	25.36	20.74	14.92	15.26	15.05

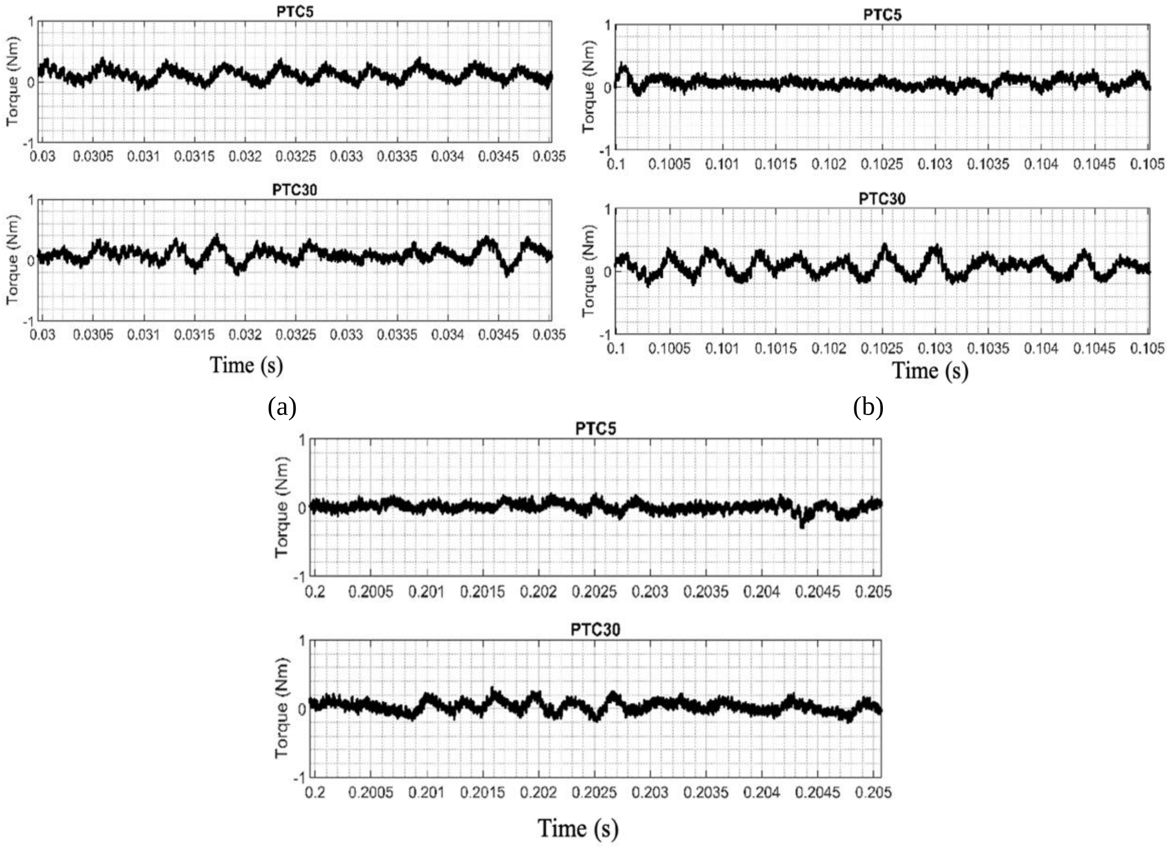

(a) (b)

(c)

Figure 7. Torque response for FCS-PTC with WF of 5 and 30 at different speeds:
(a) 30 rad/s, (b) 80 rad/s, and (c) 150 rad/s

6.2.3. Total harmonic distortion of the stator current (THD_I)

The THD of the current measures the distortion of the current waveform due to the presence of harmonics, which are multiples of the fundamental frequency. The higher the harmonics, the more distorted the current waveform. This paper analyzes the %THD for both simulation and experimental using the FFT analysis from Powergui MATLAB/ Simulink with a maximum frequency of 100kHz. Figure 8 presents the experimental results for the current waveform of both methods at three different speeds of 30 rad/s, 80 rad/s, and 150 rad/s. From these figures, it can be observed that at speeds of 30 rad/s and 80 rad/s, the PTC5 current appears to be significantly distorted compared to the PTC30. To gain more insights, Table 3 summarizes the % THD_I for the current.

It is well recognized that the THD_I is highly influenced by the torque and flux ripples of induction motor drives [25]. The flux response mainly influenced the low harmonics components of the stator current. In contrast, the torque response influenced the high harmonic components of the stator current or the switching frequency of the inverter. As shown in the study [25], it is revealed that the flux control dominates more than the torque control in determining the THD_I of the drive system. For this reason, it can be seen that the analysis of the THD_I conducted in this section for PTC5 and PTC30 produces an almost similar pattern to that obtained in the flux analysis presented in section 6.2.1. However, it gets better at high speed, which is 150 rad/s.

The results in Figure 8 depict that PTC5 exhibits the highest %THD_I, indicating the most distorted current waveform. This observation aligns with expectations, as PTC5 is also recorded to exhibit the high flux ripple at low speeds, as depicted in Figure 6. Meanwhile, PTC30 produces the lowest %THD_I at all speeds. This suggests that achieving optimal flux and torque performance using a constant WF across all speed operations is impossible. It also implies that flux control should be prioritized at lower speeds and torque control at higher speeds. This highlights the importance of selecting an appropriate WF value for each speed condition to minimize torque and flux ripple.

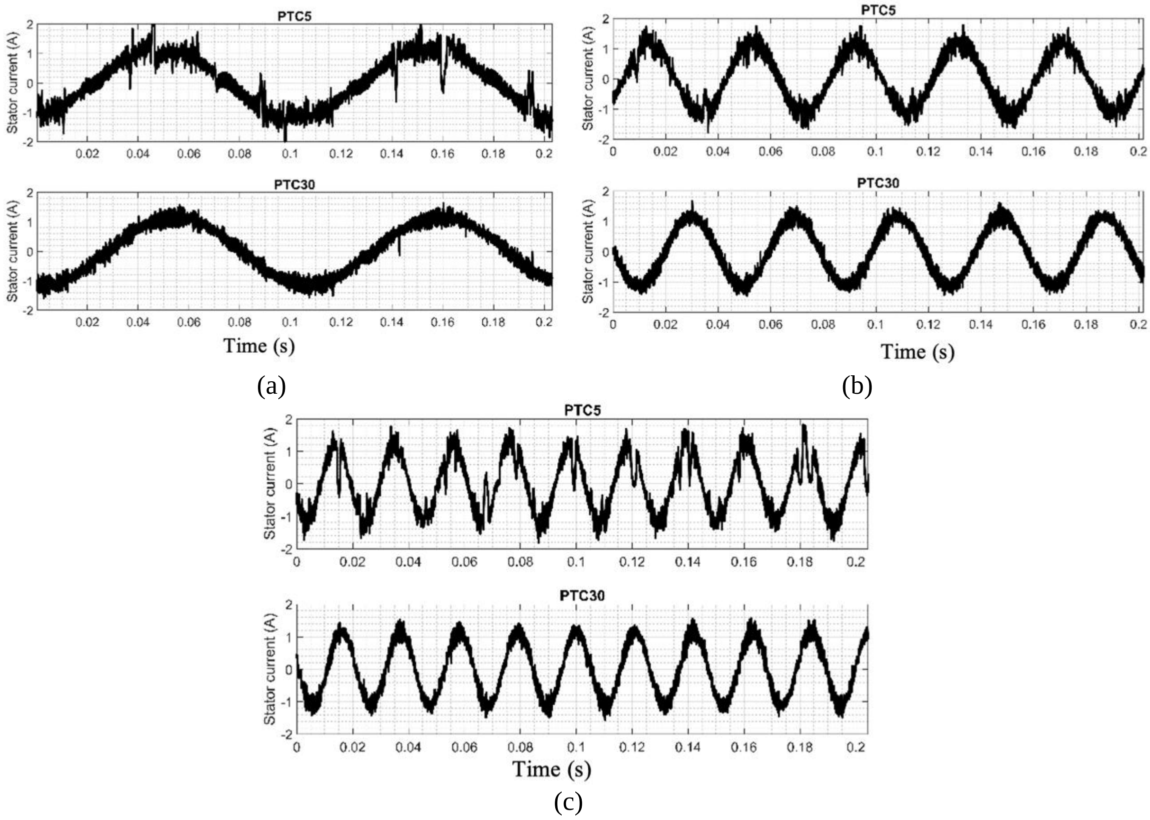

(a) (b)

(c)

Figure 8. Current waveform for FCS-PTC with WF of 5 and 30 at different speeds:
(a) 30 rad/s, (b) 80 rad/s, and (c) 150 rad/s

7. CONCLUSION

This paper provides a comprehensive hardware implementation of the FCS-PTC method. The WF used in this paper is notably low and high, emphasizing the importance of selecting an appropriate WF for the FCS-PTC drive across all speed ranges. The results indicate that a low WF can enhance torque performance; however, this negatively impacts flux control. Conversely, a high WF can improve flux performance and reduce harmonic distortion, but it may compromise torque control.

FUNDING INFORMATION

This work was supported by Universiti Teknologi Malaysia under the New Researcher Grant (Geran Penyelidik Baharu), Reference No. PY/2025/01616, Cost Center Q.J130000.2723.04K55.

AUTHOR CONTRIBUTIONS STATEMENT

This journal uses the Contributor Roles Taxonomy (CRediT) to recognize individual author contributions, reduce authorship disputes, and facilitate collaboration.

Name of Author	C	M	So	Va	Fo	I	R	D	O	E	Vi	Su	P	Fu
Rozana Alik	✓	✓	✓	✓	✓	✓		✓	✓	✓	✓		✓	✓
Nik Rumzi Nik Idris	✓	✓		✓	✓	✓	✓			✓		✓	✓	
Norjulia Mohamad Nordin		✓		✓	✓		✓			✓	✓	✓		
Tole Sutikno					✓					✓	✓			

C : **C**onceptualization
M : **M**ethodology
So : **So**ftware
Va : **Va**lidation
Fo : **Fo**rmal analysis
I : **I**nvestigation
R : **R**esources
D : **D**ata Curation
O : Writing - **O**riginal Draft
E : Writing - Review & **E**diting
Vi : **Vi**sualization
Su : **Su**pervision
P : **P**roject administration
Fu : **Fu**nding acquisition

CONFLICT OF INTEREST STATEMENT

Authors state no conflict of interest.

DATA AVAILABILITY

The data that support the findings of this study are available from the corresponding author, [RA], upon reasonable request.

REFERENCES

[1] A. M. Trzynadlowski, *Control of induction motors*. Elsevier, 2000.

[2] A. M. Trzynadlowski, *The field orientation principle in control of induction motors*, vol. 27. Springer Science & Business Media, 1993.

[3] C. Djamila and M. Yahia, “Direct torque control strategies of induction machine: Comparative studies,” in *Direct Torque Control Strategies of Electrical Machines*, IntechOpen, 2021, p. 17, doi: 10.5772/intechopen.90199.

[4] J. K. Kang and S. K. Sul, “Analysis and prediction of inverter switching frequency in direct torque control of induction machine based on hysteresis bands and machine parameters,” *IEEE Transactions on Industrial Electronics*, vol. 48, no. 3, pp. 545–553, 2001, doi: 10.1109/41.925581.

[5] I. M. Alsofyani, N. R. N. Idris, and K. B. Lee, “Dynamic hysteresis torque band for improving the performance of lookup table based DTC of induction machines,” *IEEE Transactions on Power Electronics*, vol. 33, no. 9, pp. 7959–7970, 2018, doi: 10.1109/TPEL.2017.2773129.

[6] A. K. Peter, J. Mathew, and K. Gopakumar, “A simplified DTC-SVPWM scheme for induction motor drives using a single PI controller,” *IEEE Transactions on Power Electronics*, vol. 38, no. 1, pp. 750–761, 2023, doi: 10.1109/TPEL.2022.3197362.

[7] X. Wang, Z. Wang, Z. Xu, M. Cheng, and Y. Hu, “Optimization of torque tracking performance for direct-Torque-controlled PMSM drives with composite torque regulator,” *IEEE Transactions on Industrial Electronics*, vol. 67, no. 12, pp. 10095–10108, 2020, doi: 10.1109/TIE.2019.2962451.

[8] C. Bordons and C. Montero, “Basic principles of MPC for power converters: bridging the gap between theory and practice,” *IEEE Industrial Electronics Magazine*, vol. 9, no. 3, pp. 31–43, 2015, doi: 10.1109/MIE.2014.2356600.

[9] T. Geyer, *Model Predictive Control of High-Power Converters and Industrial Drives*, John Wiley & Sons, 2016, doi: 10.1002/9781119010883.

[10] J. Rodriguez and P. Cortes, *Predictive Control of Power Converters and Electrical Drives*, John Wiley & Sons, 2012, doi: 10.1002/9781119941446.

[11] D. W. Novotny and T. A. Lipo, *Vector Control and Dynamics of AC Drives*, Oxford university press, 1996, doi: 10.1093/oso/9780198564393.001.0001.

[12] D. Finney, *Vector Control of AC Machines*, vol. 6, no. 6. Oxford University Press, USA, 1992, doi: 10.1049/pe:19920054.

[13] D. Casadei, G. Grandi, G. Serra, and A. Tani, “Switching strategies in direct torque control of induction machines,” in *The International Conference on Electrical Machines*, 1994, pp. 204–209,

[14] P. L. Jansen and R. D. Lorenz, “A physically insightful approach to the design and accuracy assessment of flux observers for field-oriented induction machine drives,” *IEEE Transactions on Industry Applications*, vol. 30, no. 1, pp. 101–110, 1993, doi: 10.1109/28.273627.

[15] M. Habibullah and D. Dah-Chuan Lu, “Stator resistance tuning for PTC based induction motor drive at very low speed,” in *2014 Australasian Universities Power Engineering Conference, AUPEC 2014 - Proceedings*, 2014, pp. 1–5, doi: 10.1109/AUPEC.2014.6966491.

[16] H. Miranda, P. Cortés, J. I. Yuz, and J. Rodríguez, “Predictive torque control of induction machines based on state-space models,” *IEEE Transactions on Industrial Electronics*, vol. 56, no. 6, pp. 1916–1924, 2009, doi: 10.1109/TIE.2009.2014904.

[17] C. A. Rojas, J. Rodriguez, F. Villarroel, J. R. Espinoza, C. A. Silva, and M. Trincado, “Predictive torque and flux control without weighting factors,” *IEEE Transactions on Industrial Electronics*, vol. 60, no. 2, pp. 681–690, 2013, doi: 10.1109/TIE.2012.2206344.

[18] J. Holtz, “Dynamic representation of AC drive systems by complex signal flow graphs,” in *IEEE International Symposium on Industrial Electronics*, 1994, pp. 1–6, doi: 10.1109/isie.1994.333121.

[19] J. Holtz and S. Stadtfeld, “Predictive Controller for the Stator Current Vector of AC machines fed from a switched voltage source,” *Proc. of IEE of Japan IPEC-Tokyo’83*, vol. 2, pp. 1665–1675, 1983.

[20] P. Cortes, J. Rodriguez, C. Silva, and A. Flores, “Delay compensation in model predictive current control of a three-phase inverter,” *IEEE Transactions on Industrial Electronics*, vol. 59, no. 2, pp. 1323–1325, 2012, doi: 10.1109/TIE.2011.2157284.

[21] P. Cortés *et al.*, “Guidelines for weighting factors design in model predictive control of power converters and drives,” in *Proceedings of the IEEE International Conference on Industrial Technology*, 2009, pp. 1–7, doi: 10.1109/ICIT.2009.4939742.

[22] S. A. Davari, V. Nekoukar, C. Garcia, and J. Rodriguez, “Online weighting factor optimization by simplified simulated annealing for finite set predictive control,” *IEEE Transactions on Industrial Informatics*, vol. 17, no. 1, pp. 31–40, 2021, doi: 10.1109/TII.2020.2981039.

[23] R. Kennel, J. Rodríguez, J. Espinoza, and M. Trincado, “High performance speed control methods for electrical machines: An assessment,” in *Proceedings of the IEEE International Conference on Industrial Technology*, 2010, pp. 1793–1799, doi: 10.1109/ICIT.2010.5472503.

[24] M. Mamdouh, M. A. Abido, and Z. Hamouz, “Weighting factor selection techniques for predictive torque control of induction motor drives: A comparison study,” *Arabian Journal for Science and Engineering*, vol. 43, no. 2, pp. 433–445, Feb. 2018, doi: 10.1007/s13369-017-2842-2.

[25] D. Casadei, G. Grandi, G. Serra, and A. Tani, “Effects of flux and torque hysteresis band amplitude in direct torque control of induction machines,” in *Proceedings of IECON’94 - 20th Annual Conference of IEEE Industrial Electronics*, IEEE, 1994, pp. 299–304, doi: 10.1109/IECON.1994.397792.

BIOGRAPHIES OF AUTHORS

Rozana Alik is a senior lecturer at the Faculty of Electrical Engineering, Universiti Teknologi Malaysia (UTM), Johor. She obtained her Ph.D. in Electrical Engineering in 2024, focusing on electric machines and predictive torque control. Before joining academia, she worked for three years as a quality engineer in the manufacturing industry. This experience shapes her practical approach to research and teaching. She holds a Master of Philosophy in solar photovoltaic systems and a bachelor's degree in electrical engineering. Her research interests include power electronics, electric drives, predictive control, and electric vehicle applications. She can be contacted at email: rozana.a@fke.utm.my.

Nik Rumzi Nik Idris received the B.Eng. degree in electrical engineering from the University of Wollongong, Wollongong, Australia, the M.Sc. degree in power electronics from Bradford University, Bradford, West Yorkshire, U.K., and the Ph.D. degree from Universiti Teknologi Malaysia, Skudai, Malaysia, in 1989, 1993, and 2000, respectively. He is a senior member of the IEEE and was a past chair (2014-2016) of the IEEE Power Electronics Malaysia Chapter. Currently, he is a professor at the Faculty of Electrical Engineering, Universiti Teknologi Malaysia, and an associate editor to the IEEE Transactions on Power Electronics. His research interests include AC drive systems and DSP applications in power electronic systems. He can be contacted at email: nikrumzi@fke.utm.my.

Norjulia Mohamad Nordin is a senior lecturer and Program Coordinator at the Faculty of Electrical Engineering. She holds a Doctor of Philosophy in Electrical Engineering from Universiti Teknologi Malaysia. She also obtained a Master's degree in Engineering Science-Energy System from the University of New South Wales, Australia, and a Bachelor's degree in Engineering (Electrical Engineering-Power) from Universiti Teknologi Malaysia in 2006. Her research expertise lies in the field of electrical engineering, particularly in the area of power electronic system. She can be contacted at email: norjulia@utm.my.

Prof. Ir. Tole Sutikno, Ph.D., MIET, IPM., ASEAN Eng. is a full professor in the Department of Electrical Engineering at Universitas Ahmad Dahlan (UAD) in Yogyakarta, Indonesia. He has held this position since 2023, having previously served as an associate professor from 2008. He earned his bachelor's degree from Universitas Diponegoro in 1999, his master's degree from Universitas Gadjah Mada in 2004, and his Ph.D. in Electrical Engineering from Universiti Teknologi Malaysia in 2016, where his doctoral research focused on advanced digital power electronics and intelligent control systems. From 2016 to 2021, he served as the Director of the Institute for Scientific Publishing and Publications (LPPI) at UAD, where he led initiatives to strengthen research visibility, journal management, and international collaboration in scholarly publishing. Since 2024, he has served as the head of the master's program in electrical engineering at UAD, following his leadership of the undergraduate program in electrical engineering in 2022. He is also the founding leader of the Embedded Systems and Power Electronics Research Group (ESPERG), which actively collaborates with both national and international institutions on topics such as fault-tolerant embedded systems, FPGA-based control, and renewable energy integration. He is widely acknowledged for his contributions to digital design, industrial electronics, motor drives, robotics, intelligent systems, and AI-based automation. His interdisciplinary research emphasizes practical deployments in industrial and healthcare contexts, covering FPGA applications, embedded systems, power electronics, and digital libraries. He has published 380 peer-reviewed articles in high-impact journals and conferences indexed by Scopus. As of 2025, Google Scholar indicates over 6,000 citations, with an h-index of 36 and an i10-index of 174. In recognition of his global research impact, he has been listed among the Top 2% of Scientists Worldwide by Stanford University and Elsevier BV from 2021 to the present, a distinction based on standardized citation metrics across all scientific disciplines. He can be contacted at email: tole@te.uad.ac.id.